Available online at www.sciencedirect.com
SCIENCE DIRECT
Journal of Power Sources 158 (2006) 333–347
JOURNAL OF POWER SOURCES
www.elsevier.com/locate/jpowsour

Exergy analysis of a solid oxide fuel cell micropowerplant

Nico Hotz, Stephan M. Senn, Dimos Poulikakos *

Laboratory of Thermodynamics in Emerging Technologies, Department of Mechanical and Process Engineering, ETH Zurich, CH-8092 Zurich, Switzerland

Received 3 April 2005; received in revised form 6 September 2005; accepted 13 September 2005
Available online 8 November 2005

Abstract

In this paper, an analytical model of a micro solid oxide fuel cell (SOFC) system fed by butane is introduced and analyzed in order to optimize its exergetic efficiency. The micro SOFC system is equipped with a partial oxidation (POX) reformer, a vaporizer, two pre-heaters, and a post-combustor. A one-dimensional (1D) polarization model of the SOFC is used to examine the effects of concentration overpotentials, activation overpotentials, and ohmic resistances on cell performance. This 1D polarization model is extended in this study to a two-dimensional (2D) fuel cell model considering convective mass and heat transport along the fuel cell channel and from the fuel cell to the environment. The influence of significant operational parameters on the exergetic efficiency of the micro SOFC system is discussed. The present study shows the importance of an exergy analysis of the fuel cell as part of an entire thermodynamic system (transportable micropowerplant) generating electric power.

Keywords: Solid oxide fuel cell; Micro SOFC system; Exergy; Butane; Partial oxidation; Efficiency

1. Introduction

Conventional power generation systems transform chemical energy of a fuel into useful electrical or mechanical power with an intermediate step of heat production. Fuel cells are a remarkable alternative for power generation transforming chemical energy directly into electric power and achieving potentially higher efficiencies than conventional power generation systems. A promising application of fuel cells are micro fuel cell systems generating electric power at the order of some watts to power mobile devices, including cell phones, cameras, and notebooks. Micro fuel cell systems have the potential to replace rechargeable batteries used in mobile devices today.

A traditional method of analyzing power generation systems is an energetic analysis applying the first law of thermodynamics. However, it is clear that instead, an exergetic analysis with exergy as the measure of the quality (useful part, transformable to work) of energy can be used to specify design optima which are different from those resulting from the energy conservation law [1]. SOFC systems have been analyzed in the sense of exergetic efficiency over the last few years. SOFC systems fed by ethanol [2–5], methane [4–7], and hydrogen [7] involving different forms of fuel reforming, i.e. steam reforming, reforming with carbon dioxide, and POX reforming, have been investigated. A point that needs improvement in these otherwise interesting studies [2–7] is the simplistic fuel cell model. Improved 1D fuel cell models accounting for polarization resistances more accurately have been developed [8,9].

The objective of the present study is, first, the extension of existing 1D polarization models [8,9] to a 2D SOFC model. This extended fuel cell model is then integrated into an entire SOFC system, which is analyzed using the approach of exergetic efficiency as also presented in [2–7]. The operational parameters of the system are chosen to match experimental data from previous studies. The objective of this study is the analytical investigation of the exergetic efficiency of the system and it is beyond the purpose of the present paper to compare the model with a real operating SOFC system. Specific requirements of an application such as a micro SOFC system generating electric power of some watts are considered in this study. The developed system is fed by butane and involves POX reforming. Butane is chosen as fuel because of its relatively easy and efficient storage in liquid phase like in small cartridges. Since the system has a modular design, different kinds of reformer as well as different fuels could be easily integrated. This study puts forth possibilities to increase

* Corresponding author. Tel.: +41 1 632 2738; fax: +41 1 632 1176.
E-mail address: dimos.poulikakos@ethz.ch (D. Poulikakos).

0378-7753/$ – see front matter © 2005 Elsevier B.V. All rights reserved.
doi:10.1016/j.jpowsour.2005.09.023

Nomenclature

a	flow availability (W)
$\bar{a}$	molar availability (J mol^{-1})
$\bar{a}^{\mathrm{chem}}$	molar chemical availability (J mol^{-1})
A	exergy flow rate (W)
b	width (m)
c	molar concentration (mol m^{-3})
D	diffusion coefficient (m^2 s^{-1})
E	cell voltage (V)
E^0	Nernst potential (V)
E_{a}, E_{c}	activation energy (J mol^{-1})
E_{el}	activation energy (J mol^{-1})
F	Faraday constant (96485 C mol^{-1})
h	absolute enthalpy including enthalpy of formation (W)
$\overline{h}$	molar absolute enthalpy including enthalpy of formation (J mol^{-1})
i	current density (A m^{-2})
i_0	exchange current density (A m^{-2})
$i^0_{0,\mathrm{a}}$, $i^0_{0,\mathrm{c}}$	pre-factor of exchange current density (A K m^{-2})
j	index
J	molar flow (mol m^{-2} s^{-1})
l	thickness (m)
L	cell length (m)
M	molar mass (g mol^{-1})
n	molar flow rate (mol s^{-1})
n_{e}	number of electrons
p	pressure (Pa)
P	power (W)
Pe	Peclet number
Pr	Prandtl number
Q	heat-transfer rate (W)
r	average pore radius (m)
R	universal gas constant (8.3145 J mol^{-1} K^{-1})
R_{el}	area-specific ohmic resistance (Ω m^2)
s	entropy (W K^{-1})
$\bar{s}$	molar absolute entropy (J mol^{-1} K^{-1})
S	surface area (m^2)
T	absolute temperature (K)
u	velocity (m s^{-1})
U	utilization factor
x	along-the-cell direction (m)
X	mole fraction
y	across-the-cell direction (m)
z	number of electrons

Greek letters

α	heat-transfer coefficient (W m^{-2} K^{-1})
δ	ratio of diffusion coefficients
ε	extension of reforming
γ	porosity
η	overpotential (V)
φ_{CO}	molar ratio between CO and CO_2
$\varphi_{\mathrm{H_2}}$	selectivity
κ	thermal diffusivity (m^2 s^{-1})
λ	molar ratio of inlet oxygen and fuel
μ	exergetic efficiency
σ	collision diameter (Å)
σ_0, σ_{el}	ionic conductivity (S m^{-1})
ξ	tortuosity
Ω	collision integral

Subscripts

a	anode
act	activation
c	cathode
conc	concentration
dest	destruction
eff	effective
el	electrolyte
h	channel
heat	heat transfer
in	inlet
irr	irreversibility
K	Knudsen
loss	loss
ohm	ohmic
out	outlet
pc	post-combustor
pox	partial oxidation reformer
pre	pre-heater
prod	production
rel	released
s	surface
sofc	solid oxide fuel cell
vap	vaporizer
0	at the standard reference state ($p = 1$ atm, $T_0 = 298$ K)

Superscripts

a	anode
c	cathode
sat	saturation
-	mole specific

the exergetic efficiency of a micro SOFC system by optimizing the operating conditions.

A major issue is to show the importance of analyzing the entire fuel cell powerplant system in the sense of exergetic efficiency instead of dealing with the fuel cell as an isolated component. Considering the micro SOFC system as a small and mobile power generating device, aspects such as storage, vaporization, and reforming of the fuel as well as heat transfer between components within a small space are essential. Analyzing only the fuel cell unit would mean neglecting these factors. The determining property of a mobile energy conversion device is the exergetic comparison between stored fuel and generated electric power. High exergetic efficiency means less fuel consumption,

smaller storage tanks, and less weight of the system, leading to a marketable design.

2. Mathematical formulation

This section presents the governing equations used to model the micro SOFC system. In Section 2.1, a 2D fuel cell model is developed. Section 2.2 introduces a model of the entire micro SOFC system.

A major approach of this study is to investigate the exergetic efficiency of the fuel cell system. An exergy balance for a control volume at steady state is formulated to calculate the exergy destruction A_{dest} of a component [10]:

$$A_{\text{dest}} = \left(1 - \frac{T_0}{T_s}\right) Q_{\text{in}} - \left(1 - \frac{T_0}{T_s}\right) Q_{\text{out}} - P + \sum_j n_{\text{in},j} \bar{a}_{\text{in},j} - \sum_j n_{\text{out},j} \bar{a}_{\text{out},j}, \quad (1)$$

using the molar flow availability $\bar{a}$ and the molar flow rate n for all species j in the inlet and outlet gas mixture. Note that T_s is the temperature of the surface at the boundary of the component where the heat fluxes Q take place and T_0 is the ambient temperature. P is the power generated in the control volume. The subscripts "in" and "out" refer to the inlets and outlets of the system component, respectively. The definition of the molar flow availability reads [10]:

$$\bar{a}_j = (\bar{h}_j(T) - \bar{h}_j(T_0)) - T_0(\bar{s}_j(T) - \bar{s}_j(T_0)) + RT_0 \ln(X_j) + \bar{a}_j^{\text{chem}}. \quad (2)$$

Note that X_j is the mole fraction of species j. The molar chemical availability $\bar{a}^{\text{chem}}$ is defined in [11]. The absolute molar enthalpies $\bar{h}$ and molar entropies $\bar{s}$ include the enthalpy and entropy of formation, respectively, and are determined from the polynomial equations [7]:

$$\bar{h} = RT\left(\beta_1 + \frac{\beta_2}{2}T + \frac{\beta_3}{3}T^2 + \frac{\beta_4}{4}T^3 + \frac{\beta_5}{5}T^4 + \frac{\beta_6}{T}\right) \quad (3)$$

and

$$\bar{s} = R\left(\beta_1 \ln(T) + \beta_2 T + \frac{\beta_3}{2}T^2 + \frac{\beta_4}{3}T^3 + \frac{\beta_5}{4}T^4 + \beta_7\right), \quad (4)$$

where the coefficients β_j can be found in JANAF tables [12].

2.1. Fuel cell

In this study, 1D across-the-cell models developed by Zhu and Kee [8] and Chan et al. [7,9] are used and extended to a 2D along-the-channel model. These existing 1D models [7–9] represent a unit cell of a membrane electrode assembly (MEA) and describe the diffusive mass transport and electrochemical processes. Fluid flow and species transport along the channels as well as heat transfer are neglected in these models. In order to get a better idea of a realistic fuel cell, a 1D polarization model is incorporated as a submodel into a 2D fuel cell model considering convective mass transport along channels and heat transport in both dimensions. Local current densities can change substantially along a fuel cell channel as a result of fuel and oxygen depletion. 1D models disregard this aspect.

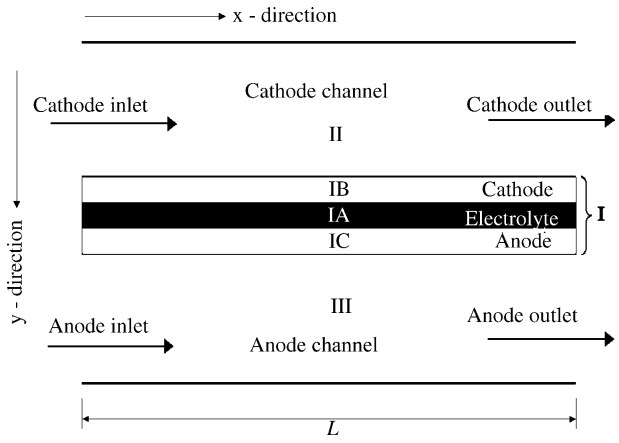

Fig. 1. Schematic of the fuel cell.

2.1.1. Across-the-cell direction

The fuel cell is modeled as a system of three components: a cathode channel, an anode channel, and an MEA. The MEA consists of a cathode, an anode, and an electrolyte in between. Fuel and air are transported along the channels (x-direction in Fig. 1). Due to the high Peclet numbers $Pe_D = uL/D$ and $Pe_\kappa = uL/\kappa$, mass and heat diffusion along the channel direction can be neglected. In this study, the Peclet number Pe_D is at the order of 5×10^3 for the anode and cathode channels, and the thermal Peclet number Pe_κ is at the order of 10^3. In the y-direction across the MEA, reactants and products of the fuel cell reactions are transported by diffusion (see Fig. 1). The gas mixtures in the cathode and anode channels (II and III) are assumed to be well mixed. Therefore, the conditions at the boundary of the channels are the same as the bulk conditions. The temperature only varies along the x-direction, it is assumed to be constant in the y-direction. Oxygen diffuses from the cathode channel (II) through the porous cathode (IB). At the interface between the porous cathode (IB) and the electrolyte (IA), oxygen is reduced to oxygen ions O^{2-} and the ions are transported through the electrolyte. On the other side, hydrogen diffuses from the anode channel (III) through the porous anode (IC) to the electrolyte/anode interface, where hydrogen reacts with oxygen ions to form water, the product of the global fuel cell reaction.

The cell voltage is mainly affected by activation barriers for electrochemical reactions and by resistances to mass transfer. Mass transfer includes the diffusion of gases in the porous electrodes and the transport of oxygen ions in the electrolyte. The resistances are called activation polarizations of the anode and the cathode, concentration polarizations of the anode and cathode, and ohmic polarization of the electrolyte.

The cell voltage E can be calculated using the energy balance of a differential part of the fuel cell,

$$\mathrm{d}P + \mathrm{d}Q_{\text{h}} + \mathrm{d}h_{\text{h}}^{\text{c}} + \mathrm{d}h_{\text{h}}^{\text{a}} = 0, \quad (5)$$

and the entropy balance,

$$\mathrm{d}s_{\mathrm{prod}} - T^{-1}\mathrm{d}Q_{\mathrm{h}} - \mathrm{d}s_{\mathrm{h}}^{\mathrm{c}} - \mathrm{d}s_{\mathrm{h}}^{\mathrm{a}} = 0, \tag{6}$$

where $\mathrm{d}Q_h$ and $\mathrm{d}P$ are the differential heat-transfer rate and the differential power, respectively. The differential $\mathrm{d}s_{\mathrm{prod}}$ is the differential entropy production due to irreversible processes in the fuel cell. The cathode and anode flows consist of different species j. The enthalpy and entropy are calculated by:

$$h_{\mathrm{h}} = \sum_j n_j \bar{h}_j \tag{7}$$

and

$$s_{\mathrm{h}} = \sum_j n_j \bar{s}_j, \tag{8}$$

respectively, with molar flow rates indicated by n. The absolute molar enthalpies $\bar{h}$ and molar entropies $\bar{s}$ include the enthalpy and entropy of formation, respectively, and are determined from Eqs. (3) and (4). Combining Eqs. (5) and (6), the differential electric power $\mathrm{d}P$ reads:

$$\mathrm{d}P = -(\mathrm{d}h_{\mathrm{h}}^{\mathrm{c}} - T\mathrm{d}s_{\mathrm{h}}^{\mathrm{c}}) - (\mathrm{d}h_{\mathrm{h}}^{\mathrm{a}} - T\mathrm{d}s_{\mathrm{h}}^{\mathrm{a}}) - T\mathrm{d}s_{\mathrm{prod}}. \tag{9}$$

Since $\mathrm{d}P$ is the electric power generated by the fuel cell, it can be written as:

$$\mathrm{d}P = zFE\,\mathrm{d}n_{\mathrm{H_2}}, \tag{10}$$

where z is the number of electrons, $\mathrm{d}n_{\mathrm{H_2}}$ is the molar flow rate of hydrogen participating in the reaction in the differential fuel cell part, and F is the Faraday constant [9]. The global fuel cell reaction reads:

$$2\mathrm{H_2} + \mathrm{O_2} \rightarrow 2\mathrm{H_2O}. \tag{11}$$

The differential electric power is therefore given as:

$$\mathrm{d}P = 2FE\,\mathrm{d}n_{\mathrm{H_2}}. \tag{12}$$

Combination of Eqs. (9) and (12) results in:

$$E = -\frac{1}{2F}\left(\frac{\mathrm{d}h_{\mathrm{h}}^{\mathrm{c}}}{\mathrm{d}n_{\mathrm{H_2}}} + \frac{\mathrm{d}h_{\mathrm{h}}^{\mathrm{a}}}{\mathrm{d}n_{\mathrm{H_2}}}\right) + \frac{T}{2F}\left(\frac{\mathrm{d}s_{\mathrm{h}}^{\mathrm{c}}}{\mathrm{d}n_{\mathrm{H_2}}} + \frac{\mathrm{d}s_{\mathrm{h}}^{\mathrm{a}}}{\mathrm{d}n_{\mathrm{H_2}}}\right) - \frac{T}{2F}\frac{\mathrm{d}s_{\mathrm{prod}}}{\mathrm{d}n_{\mathrm{H_2}}}. \tag{13}$$

The first two terms of the right-hand side represent the ideal cell potential, the Nernst potential E^0, and the last term describes the voltage drop due to polarizations in the fuel cell. The cell voltage E reads therefore as the difference between the Nernst potential E^0 and the sum of all polarizations η_{tot}, given by:

$$E = E^0 - \eta_{\mathrm{tot}}. \tag{14}$$

The sum of all polarizations in the fuel cell η_{tot} can be written as:

$$\eta_{\mathrm{tot}} = \eta_{\mathrm{act,a}} + \eta_{\mathrm{act,c}} + \eta_{\mathrm{conc,a}} + \eta_{\mathrm{conc,c}} + \eta_{\mathrm{ohm}}. \tag{15}$$

The activation polarizations $\eta_{\mathrm{act,a}}$ and $\eta_{\mathrm{act,c}}$, the concentration polarizations $\eta_{\mathrm{conc,a}}$ and $\eta_{\mathrm{conc,c}}$, and the ohmic polarization of the electrolyte η_{ohm} are modeled based on [7–9]. The detailed model is listed in the appendix.

2.1.2. Along-the-channel direction

2.1.2.1. Membrane electrode assembly. A mass balance of the molar diffusion fluxes across the boundaries of the MEA reads:

$$J_{\mathrm{H_2}} = J_{\mathrm{H_2O}} = 2J_{\mathrm{O_2}}, \tag{16}$$

using stoichiometry from Eq. (11). The molar fluxes J are proportional to the current density i, i.e.,

$$J_{\mathrm{H_2}} = \frac{i}{2F}, \tag{17}$$

$$J_{\mathrm{H_2O}} = \frac{i}{2F}, \tag{18}$$

and

$$J_{\mathrm{O_2}} = \frac{i}{4F}. \tag{19}$$

The energy balance of the MEA takes into account enthalpy transport by diffusion and the generated electric power. There is no heat flux between the MEA and the surrounding channels, since they are at the same temperature. According to Fig. 2, the energy balance can be formulated as:

$$\mathrm{d}h_{J_{\mathrm{H_2}}} + \mathrm{d}h_{J_{\mathrm{O_2}}} = \mathrm{d}h_{J_{\mathrm{H_2O}}} + \mathrm{d}P, \tag{20}$$

where $\mathrm{d}h_{J_{\mathrm{H_2}}}$, $\mathrm{d}h_{J_{\mathrm{O_2}}}$, and $\mathrm{d}h_{J_{\mathrm{H_2O}}}$ account for enthalpy transport by species diffusion, and $\mathrm{d}P$ is the generated electric power. Note that:

$$\mathrm{d}h_{J_{\mathrm{H_2}}} = J_{\mathrm{H_2}}\bar{h}_{\mathrm{H_2}} b\,\mathrm{d}x, \tag{21}$$

$$\mathrm{d}h_{J_{\mathrm{O_2}}} = J_{\mathrm{O_2}}\bar{h}_{\mathrm{O_2}} b\,\mathrm{d}x, \tag{22}$$

and

$$\mathrm{d}h_{J_{\mathrm{H_2O}}} = J_{\mathrm{H_2O}}\bar{h}_{\mathrm{H_2O}} b\,\mathrm{d}x \tag{23}$$

applies, where b is the electrolyte width (measured perpendicular to x and y) and $\bar{h}$ is the molar absolute enthalpy in J mol^{-1}. The

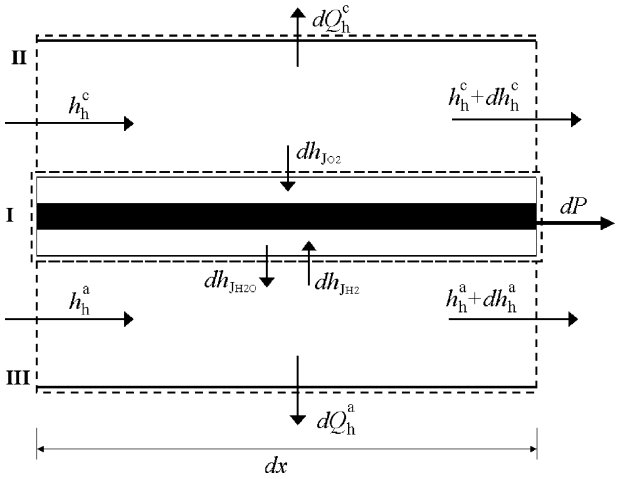

Fig. 2. Schematic of energy transfer in the fuel cell.

generated electric power dP reads:

$$\mathrm{d}P = Eib\,\mathrm{d}x. \tag{24}$$

2.1.2.2. Cathode channel. For the cathode channel, a mass balance and an energy balance can be formulated. The molar flow rate of nitrogen in the channel is constant, since nitrogen is not converted in the cell reaction. The molar flow rate of oxygen $n_{\mathrm{O_2}}$ decreases along the channel according to:

$$\frac{\mathrm{d}n_{\mathrm{O_2}}}{\mathrm{d}x} = -bJ_{\mathrm{O_2}}. \tag{25}$$

The differential energy balance of the cathode channel can be written as (see Fig. 2):

$$\frac{\mathrm{d}h_{\mathrm{h}}^{\mathrm{c}}}{\mathrm{d}x} = -\frac{\mathrm{d}Q_{\mathrm{h}}^{\mathrm{c}}}{\mathrm{d}x} - \frac{\mathrm{d}h_{J_{\mathrm{O_2}}}}{\mathrm{d}x}. \tag{26}$$

The absolute enthalpy of the mass flow in the cathode channel reads:

$$h_{\mathrm{h}}^{\mathrm{c}} = \sum_j n_j \bar{h}_{\mathrm{h},j}^{\mathrm{c}}, \tag{27}$$

where j refers to the species oxygen and nitrogen. The molar absolute enthalpy $\bar{h}$ is defined by Eq. (3). For the heat loss from the cathode channel to the environment,

$$\frac{\mathrm{d}Q_{\mathrm{h}}^{\mathrm{c}}}{\mathrm{d}x} = \alpha_{\mathrm{h}}^{\mathrm{c}} b(T_{\mathrm{sofc}}(x) - T_0) \tag{28}$$

applies, where $\alpha_{\mathrm{h}}^{\mathrm{c}}$ is the heat-transfer coefficient between the cathode channel and the environment.

2.1.2.3. Anode channel. Species conservation for hydrogen and water in the anode channel leads to:

$$\frac{\mathrm{d}n_{\mathrm{H_2}}}{\mathrm{d}x} = -bJ_{\mathrm{H_2}} \tag{29}$$

and

$$\frac{\mathrm{d}n_{\mathrm{H_2O}}}{\mathrm{d}x} = bJ_{\mathrm{H_2O}}, \tag{30}$$

respectively. Conservation of energy in the anode channel reads:

$$\frac{\mathrm{d}h_{\mathrm{h}}^{\mathrm{a}}}{\mathrm{d}x} = -\frac{\mathrm{d}Q_{\mathrm{h}}^{\mathrm{a}}}{\mathrm{d}x} - \frac{\mathrm{d}h_{J_{\mathrm{H_2}}}}{\mathrm{d}x} + \frac{\mathrm{d}h_{J_{\mathrm{H_2O}}}}{\mathrm{d}x}. \tag{31}$$

The absolute enthalpy of the mass flow in the anode channel is written as:

$$h_{\mathrm{h}}^{\mathrm{a}} = \sum_j n_j \bar{h}_{\mathrm{h},j}^{\mathrm{a}}, \tag{32}$$

where j refers to the species hydrogen, water, oxygen, nitrogen, butane, carbon dioxide, and carbon monoxide in the anode channel. For the heat loss from the anode channel to the environment,

$$\frac{\mathrm{d}Q_{\mathrm{h}}^{\mathrm{a}}}{\mathrm{d}x} = \alpha_{\mathrm{h}}^{\mathrm{a}} b(T_{\mathrm{sofc}}(x) - T_0) \tag{33}$$

applies, where $\alpha_{\mathrm{h}}^{\mathrm{a}}$ is the heat-transfer coefficient between the anode channel and the environment.

2.1.2.4. Entire fuel cell. The heat loss from the channels to the environment dQ_{h} [see Eqs. (5) and (6)] is given by

$$\mathrm{d}Q_{\mathrm{h}} = \mathrm{d}Q_{\mathrm{h}}^{\mathrm{c}} + \mathrm{d}Q_{\mathrm{h}}^{\mathrm{a}}. \tag{34}$$

An exergy balance around the entire fuel cell, including the MEA, the anode channel, and the cathode channel, is formulated to compute the exergy destruction A_{dest}, given by:

$$\frac{\mathrm{d}A_{\mathrm{dest}}}{\mathrm{d}x} = -\left(1 - \frac{T_0}{T_{\mathrm{sofc}}(x)}\right)\frac{\mathrm{d}Q_{\mathrm{h}}}{\mathrm{d}x} - \frac{\mathrm{d}P}{\mathrm{d}x} - \frac{\mathrm{d}a_{\mathrm{h}}^{\mathrm{c}}}{\mathrm{d}x} - \frac{\mathrm{d}a_{\mathrm{h}}^{\mathrm{a}}}{\mathrm{d}x}, \tag{35}$$

where the availability of the mass flow in the cathode and the anode channel read:

$$a_{\mathrm{h}}^{\mathrm{c}} = \sum_j n_j \bar{a}_{\mathrm{h},j}^{\mathrm{c}} \tag{36}$$

and

$$a_{\mathrm{h}}^{\mathrm{a}} = \sum_j n_j \bar{a}_{\mathrm{h},j}^{\mathrm{a}}, \tag{37}$$

respectively. The definition of the molar flow availability is given by Eq. (2).

2.2. Micro SOFC system

A thermodynamic model of a micro SOFC, including a POX reformer, a post-combustor, a vaporizer, and two pre-heaters, arranged according to Fig. 3, is presented in this subsection. The vaporizer is needed to provide gaseous butane. The reformer converts butane by POX to hydrogen and carbon monoxide. Air and butane are preheated. The exhaust gases of the SOFC can be burnt in a post-combustor to provide heat for preheating and to avoid exhaust of carbon monoxide and unburnt hydrocarbons. The POX reformer, the SOFC, and the post-combustor generate heat. The vaporizer and the pre-heaters require heat, part of which may be lost to the environment. The components of the system are modeled as control volumes, except the fuel cell, which is modeled according to the previous subsection. The heat transport within the system is shown in Fig. 3. The heat released from the SOFC is rejected to the environment, whereas the heat released from the POX reformer and the post-combustor is used to heat the two pre-heaters and the vaporizer. The post-combustor is assumed to provide the heat required in pre-heater 1 and the vaporizer, and the POX reformer is assumed to provide the heat for pre-heater 2. If the POX reformer and the post-combustor release more heat than required by the pre-heaters and the vaporizer, the waste heat will be released to the environment. The results will show that indeed the amount of heat released is higher than that needed for the pre-heaters and the vaporizer. Therefore, even for a low efficiency of heat exchange between the components of the micro SOFC system, the necessary heat transfer within the system can be achieved.

According to Fig. 3, the heat exchange between the components and the environment can be formulated as:

$$Q_{\mathrm{rel1}} = Q_{\mathrm{pc}} - Q_{\mathrm{pre1}} - Q_{\mathrm{vap}}, \tag{38}$$

$$Q_{\mathrm{rel2}} = Q_{\mathrm{pox}} - Q_{\mathrm{pre2}}, \tag{39}$$

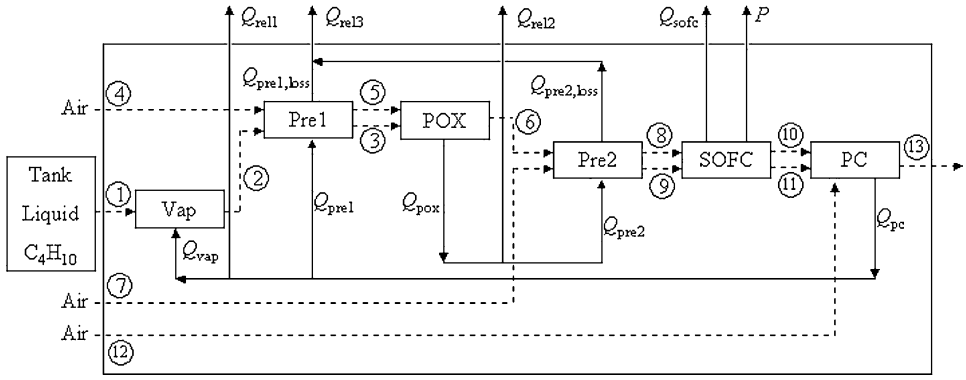

Fig. 3. Schematic of the entire micro SOFC system.

and

$$Q_{rel3} = Q_{pre1,loss} + Q_{pre2,loss}, \tag{40}$$

where the total heat flux released from the system to the environment reads:

$$Q_{rel} = Q_{rel1} + Q_{rel2} + Q_{rel3} + Q_{sofc}. \tag{41}$$

The total exergy destruction by irreversibilities in the system reads:

$$A_{dest,irr} = A_{dest,vap} + A_{dest,pre1} + A_{dest,pox} + A_{dest,pre2} + A_{dest,sofc} + A_{dest,pc}, \tag{42}$$

where the exergy destruction by heat transfer $A_{dest,heat}$ is calculated implicitly by:

$$A_{dest,heat} = a_1 + a_4 + a_7 + a_{12} - a_{13} - P - A_{dest,irr}. \tag{43}$$

2.2.1. Conservation laws

For every component of the system, a mass balance, an energy balance, and an exergy balance can be formulated. Conservation of mass at steady state for a certain system component requires that the inlet flow rates of hydrogen, carbon, oxygen, and nitrogen have to be the same as the outlet flow rates, i.e.,

$$\sum_j n_{in,j} = \sum_j n_{out,j}, \tag{44}$$

where j refers to the elements H, C, O, and N. Other elements are neglected in this study, since pure butane is used as fuel and air is assumed to consist of 21% oxygen and 79% nitrogen. Humidity and carbon dioxide in the air are neglected.

The pressure is assumed to be constant at atmospheric state, except for the pressure in the storage tank of liquid butane. The change of kinetic and potential energy is neglected. The energy balance of a certain system component then reads:

$$\sum_j \bar{h}_{in,j} n_{in,j} + Q_{in} = \sum_j \bar{h}_{out,j} n_{out,j} + Q_{out} + P, \tag{45}$$

where $\bar{h}$ is the molar absolute enthalpy, n is a molar flow rate, Q a heat flux, and P the generated power. The molar absolute enthalpies $\bar{h}$ include the enthalpy of formation and are calculated using the JANAF tables [12] according to Eq. (3).

An exergy balance, defined by Eq. (1), is formulated to calculate the exergy destruction A_{dest} of a component and to determine the exergetic efficiency of the processes in each system component.

2.2.2. Vaporizer

In the vaporizer, the liquid butane at a storage pressure p_1 is expanded isothermally to gaseous butane at p_0. The vaporizer is modeled as isothermal at the ambient temperature, therefore the temperatures:

$$T_1 = T_2 = T_{vap} = T_0 \tag{46}$$

are identical. The molar flow rate of butane remains unchanged in the vaporizer, and the mass balance of the vaporizer results in:

$$n_{C_4H_{10},1} = n_{C_4H_{10},2}. \tag{47}$$

The energy balance reads:

$$Q_{vap} = n_{C_4H_{10},1}(\bar{h}_2 - \bar{h}_1), \tag{48}$$

where $\bar{h}_1$ is the molar enthalpy of liquid butane at pressure p_1 and temperature T_0 [13]. The molar enthalpy of gaseous butane $\bar{h}_2$ is calculated according to Eq. (3). The exergy balance is given by:

$$A_{dest,vap} = \left(1 - \frac{T_0}{T_{vap}}\right) Q_{vap} + n_{C_4H_{10},1}(\bar{a}_1 - \bar{a}_2), \tag{49}$$

where $\bar{a}_1$ is the molar flow availability of liquid butane at pressure p_1 and temperature T_0. According to Eq. (2), the molar flow availability $\bar{a}_1$ is calculated as:

$$\bar{a}_1 = (\bar{h}_1 - \bar{h}_2) - T_0(\bar{s}_1 - \bar{s}_2) + \bar{a}^{chem}_{C_4H_{10}}, \tag{50}$$

since state 2 is at ambient temperature T_0. The molar entropy of liquid butane $\bar{s}_1$ is taken from [13].

2.2.3. Pre-heaters

The pre-heaters have two inlets and two outlets to preheat two gas flows without mixing them. In the pre-heater 1, air and gaseous butane are preheated separately. In the pre-heater 2, air and the fuel gas mixture are preheated. The pre-heaters allow heat exchange between both gas flows. The temperature at the outlets is assumed to be identical such that $T_3 = T_5$ and $T_8 = T_9$.

A mean pre-heater temperature is defined as:

$$T_{\mathrm{pre}} = \frac{T_{\mathrm{in,pre}} + T_{\mathrm{out}}}{2}, \tag{51}$$

where $T_{\mathrm{in,pre}}$ is given by the implicit formulation

$$n_{\mathrm{C_4H_{10},2}}\bar{h}_{\mathrm{C_4H_{10}}}(T_{\mathrm{in,pre1}}) + n_{\mathrm{air,4}}\bar{h}_{\mathrm{air}}(T_{\mathrm{in,pre1}}) = n_{\mathrm{C_4H_{10},2}}\bar{h}_{\mathrm{C_4H_{10}}}(T_2) + n_{\mathrm{air,4}}\bar{h}_{\mathrm{air}}(T_4) \tag{52}$$

for pre-heater 1, and

$$n_6\bar{h}_6(T_{\mathrm{in,pre2}}) + n_{\mathrm{air,7}}\bar{h}_{\mathrm{air}}(T_{\mathrm{in,pre2}}) = n_6\bar{h}_6(T_6) + n_{\mathrm{air,7}}\bar{h}_{\mathrm{air}}(T_7) \tag{53}$$

for pre-heater 2. The heat released to the environment

$$Q_{\mathrm{pre,loss}} = \alpha_{\mathrm{pre}} S_{\mathrm{pre}}(T_{\mathrm{pre}} - T_0) \tag{54}$$

is assumed to depend on the difference between the mean pre-heater temperature and the ambient temperature, where α_{pre} is a heat-transfer coefficient between the surface S_{pre} of the pre-heater and the environment. The necessary heat input for the first pre-heater Q_{pre1} reads:

$$Q_{\mathrm{pre1}} = Q_{\mathrm{pre1,loss}} + n_{\mathrm{C_4H_{10},3}}(\bar{h}_{\mathrm{C_4H_{10},3}} - \bar{h}_{\mathrm{C_4H_{10},2}}) + n_{\mathrm{air,5}}(\bar{h}_{\mathrm{air,5}} - \bar{h}_{\mathrm{air,4}}) \tag{55}$$

and the necessary heat input for the pre-heater 2 reads:

$$Q_{\mathrm{pre2}} = Q_{\mathrm{pre2,loss}} + \sum_j n_{6,j}(\bar{h}_{8,j} - \bar{h}_{6,j}) + n_{\mathrm{air,7}}(\bar{h}_{\mathrm{air,9}} - \bar{h}_{\mathrm{air,7}}). \tag{56}$$

The pre-heater 1 is heated by the post-combustor. The exergy destruction is given by:

$$A_{\mathrm{dest,pre1}} = \left(1 - \frac{T_0}{T_{\mathrm{pre1}}}\right)(Q_{\mathrm{pre1}} - Q_{\mathrm{pre1,loss}}) + n_{\mathrm{C_4H_{10},2}}(\bar{a}_{\mathrm{C_4H_{10},2}} - \bar{a}_{\mathrm{C_4H_{10},3}}) + n_{\mathrm{air,5}}(\bar{a}_{\mathrm{air,4}} - \bar{a}_{\mathrm{air,5}}). \tag{57}$$

The pre-heater 2 is heated by the POX reformer. The exergy destruction is given by:

$$A_{\mathrm{dest,pre2}} = \left(1 - \frac{T_0}{T_{\mathrm{pre2}}}\right)(Q_{\mathrm{pre2}} - Q_{\mathrm{pre2,loss}}) + \sum_j n_{6,j}(\bar{a}_{6,j} - \bar{a}_{8,j}) + n_{9,\mathrm{air}}(\bar{a}_{7,\mathrm{air}} - \bar{a}_{9,\mathrm{air}}). \tag{58}$$

2.2.4. POX reformer

The POX reformer has two separate inlets, one for preheated air (state 5) and one for vaporized butane (state 3). The reforming reaction is given as:

$$\mathrm{C_4H_{10}} + \lambda_{\mathrm{pox}}\mathrm{O_2} + 3.76\lambda_{\mathrm{pox}}\mathrm{N_2} \rightarrow 5\varepsilon\varphi_{\mathrm{H_2}}\mathrm{H_2} + \frac{4\varepsilon\varphi_{\mathrm{CO}}}{1+\varphi_{\mathrm{CO}}}\mathrm{CO} + \frac{4\varepsilon}{1+\varphi_{\mathrm{CO}}}\mathrm{CO_2} + 5\varepsilon(1-\varphi_{\mathrm{H_2}})\mathrm{H_2O} + \left(\lambda_{\mathrm{pox}} - 2\varepsilon\frac{2+\varphi_{\mathrm{CO}}}{1+\varphi_{\mathrm{CO}}} - \frac{5\varepsilon}{2}(1-\varphi_{\mathrm{H_2}})\right) \times \mathrm{O_2} + 3.76\lambda_{\mathrm{pox}}\mathrm{N_2} + (1-\varepsilon)\mathrm{C_4H_{10}}, \tag{59}$$

where λ_{pox} is the air/fuel ratio of the POX reformer, φ_{CO} the molar ratio of carbon monoxide and carbon dioxide, $\varphi_{\mathrm{H_2}}$ the selectivity of the reforming process for hydrogen, and ε the extension of reforming. The latter is the fraction of butane converted in the reformer, given as:

$$\varepsilon = \frac{n_{\mathrm{C_4H_{10},3}} - n_{\mathrm{C_4H_{10},6}}}{n_{\mathrm{C_4H_{10},3}}}. \tag{60}$$

The ratio

$$\lambda_{\mathrm{pox}} = \frac{n_{\mathrm{O_2,5}}}{n_{\mathrm{C_4H_{10},3}}} \tag{61}$$

relates the inlet flow rate of oxygen to the inlet flow rate of butane. The parameter φ_{CO} reads:

$$\varphi_{\mathrm{CO}} = \frac{n_{\mathrm{CO,6}}}{n_{\mathrm{CO_2,6}}} \tag{62}$$

at the outlet. The selectivity of the reforming process for hydrogen $\varphi_{\mathrm{H_2}}$ is given by:

$$\varphi_{\mathrm{H_2}} = \frac{(1/5)n_{\mathrm{H_2,6}}}{n_{\mathrm{C_4H_{10},3}} - n_{\mathrm{C_4H_{10},6}}}. \tag{63}$$

A mean temperature of the POX reformer is defined as:

$$T_{\mathrm{pox}} = \frac{T_{\mathrm{in,pox}} + T_6}{2}, \tag{64}$$

where $T_{\mathrm{in,pox}}$ is given by the implicit formulation:

$$n_{\mathrm{C_4H_{10},3}}\bar{h}_{\mathrm{C_4H_{10}}}(T_{\mathrm{in,pox}}) + n_{\mathrm{air,5}}\bar{h}_{\mathrm{air}}(T_{\mathrm{in,pox}}) = n_{\mathrm{C_4H_{10},3}}\bar{h}_3(T_3) + n_{\mathrm{air,5}}\bar{h}_5(T_5). \tag{65}$$

The energy balance reads:

$$Q_{\mathrm{pox}} + n_6\bar{h}_6 = n_{\mathrm{C_4H_{10},3}}\bar{h}_3 + n_{\mathrm{air,5}}\bar{h}_5 \tag{66}$$

and the exergy balance reads:

$$A_{\mathrm{dest,pox}} = -\left(1 - \frac{T_0}{T_{\mathrm{pox}}}\right)Q_{\mathrm{pox}} + n_{\mathrm{C_4H_{10},3}}\bar{a}_{\mathrm{C_4H_{10},3}} + n_{\mathrm{air,5}}\bar{a}_{\mathrm{air,5}} - n_{\mathrm{H_2,6}}\bar{a}_{\mathrm{H_2,6}} - n_{\mathrm{C_4H_{10},6}}\bar{a}_{\mathrm{C_4H_{10},6}} - n_{\mathrm{O_2,6}}\bar{a}_{\mathrm{O_2,6}} - n_{\mathrm{N_2,6}}\bar{a}_{\mathrm{N_2,6}} - n_{\mathrm{CO_2,6}}\bar{a}_{\mathrm{CO_2,6}} - n_{\mathrm{CO,6}}\bar{a}_{\mathrm{CO,6}} - n_{\mathrm{H_2O,6}}\bar{a}_{\mathrm{H_2O,6}}. \tag{67}$$

2.2.5. Solid oxide fuel cell

For the SOFC, the model presented in Section 2.1 is used. The inlet fuel is at state 8, and the inlet air is at state 9. The anode and cathode outlets are states 10 and 11, respectively. An important performance parameter of the fuel cell is the utilization factor of hydrogen,

$$U_{\mathrm{H_2}} = \frac{n_{\mathrm{H_2,8}} - n_{\mathrm{H_2,10}}}{n_{\mathrm{H_2,8}}}, \tag{68}$$

indicating the amount of hydrogen that is converted in the fuel cell. The parameter

$$\lambda_{\text{sofc}} = \frac{n_{\text{O}_2,9}}{n_{\text{H}_2,8}/2} \tag{69}$$

is the molar ratio between oxygen and stoichiometric oxygen at the fuel cell inlet. Using the utilization factor of hydrogen, a mass balance for hydrogen in the anode channel results in

$$n_{\text{H}_2,10} = n_{\text{H}_2,8}(1 - U_{\text{H}_2}). \tag{70}$$

Species conservation for water in the anode channel leads to:

$$n_{\text{H}_2\text{O},10} = n_{\text{H}_2\text{O},8} + n_{\text{H}_2,8}U_{\text{H}_2}. \tag{71}$$

A mass balance for oxygen in the cathode channel requires:

$$n_{\text{O}_2,11} = \frac{n_{\text{O}_2,9} - n_{\text{H}_2,8}U_{\text{H}_2}}{2}. \tag{72}$$

All other species have constant molar flow rates since they do not react in the fuel cell. The total heat released to the environment is written as:

$$Q_{\text{sofc}} = Q_{\text{h}}^{\text{c}} + Q_{\text{h}}^{\text{a}}. \tag{73}$$

The heat released from the cathode and the anode channel is calculated by:

$$Q_{\text{h}}^{\text{c}} = \alpha_{\text{h}}^{\text{c}} b \int_0^L (T_{\text{sofc}}(x) - T_0)\,\text{d}x \tag{74}$$

and

$$Q_{\text{h}}^{\text{a}} = \alpha_{\text{h}}^{\text{a}} b \int_0^L (T_{\text{sofc}}(x) - T_0)\,\text{d}x, \tag{75}$$

using Eqs. (28) and (33), respectively. An essential parameter of this study is the exergetic efficiency μ of the entire micro SOFC system, defined as the ratio between the exergy output (i.e., the electric power P) and the exergy input (i.e., the flow availability of butane at state 1 and air at the states 4, 7, and 12), given as:

$$\mu = \frac{P}{a_1 + a_4 + a_7 + a_{12}}, \tag{76}$$

where the electric power reads:

$$P = Eb \int_0^L i(x)\,\text{d}x, \tag{77}$$

according to Eq. (24).

2.2.6. Post-combustor

In the post-combustor, the remaining butane, hydrogen, and carbon monoxide from the fuel cell exhaust are burnt, such that,

$$n_{\text{H}_2,13} = n_{\text{CO},13} = n_{\text{C}_4\text{H}_{10},13} = 0. \tag{78}$$

As a result, the species conservation equations,

$$n_{\text{CO}_2,13} = 4n_{\text{C}_4\text{H}_{10},1} \tag{79}$$

and

$$n_{\text{H}_2\text{O},13} = 5n_{\text{C}_4\text{H}_{10},1} \tag{80}$$

can be formulated in the post-combustor.

If $n_{\text{O}_2,4} + n_{\text{O}_2,7} < (13/2)n_{\text{C}_4\text{H}_{10},1}$, the remaining oxygen from the fuel cell is not enough for total combustion of butane, hydrogen, and carbon monoxide in the exhaust gas. In this case, more air is provided at state 12. The necessary molar flow rate at the inlet 12 is given by:

$$n_{\text{O}_2,12} = \left(\frac{13}{2}\right) n_{\text{C}_4\text{H}_{10},1} - n_{\text{O}_2,4} - n_{\text{O}_2,7}, \tag{81}$$

such that

$$n_{\text{O}_2,13} = 0. \tag{82}$$

If $n_{\text{O}_2,4} + n_{\text{O}_2,7} \geq (13/2)n_{\text{C}_4\text{H}_{10},1}$, the unburnt oxygen from the POX reformer and the fuel cell is enough for total combustion of butane, hydrogen, and carbon monoxide in the exhaust gas. The remaining oxygen in the outlet is in this case:

$$n_{\text{O}_2,13} = n_{\text{O}_2,4} + n_{\text{O}_2,7} - \left(\frac{13}{2}\right) n_{\text{C}_4\text{H}_{10},1}, \tag{83}$$

where $n_{\text{O}_2,12} = 0$. The molar flow rate of nitrogen in the outlet gas reads:

$$n_{\text{N}_2,13} = 3.76(n_{\text{O}_2,4} + n_{\text{O}_2,7} + n_{\text{O}_2,12}). \tag{84}$$

A mean temperature of the post-combustor is defined as:

$$T_{\text{pc}} = \frac{T_{\text{in,pc}} + T_{13}}{2}, \tag{85}$$

where $T_{\text{in,pc}}$ is given by the implicit formulation:

$$\begin{aligned} &n_{10}\bar{h}_{10}(T_{\text{in,pc}}) + n_{11}\bar{h}_{11}(T_{\text{in,pc}}) + n_{12}\bar{h}_{12}(T_{\text{in,pc}}) \\ &\quad = n_{10}\bar{h}_{10}(T_{10}) + n_{11}\bar{h}_{11}(T_{11}) + n_{12}\bar{h}_{12}(T_{12}). \end{aligned} \tag{86}$$

Conservation of energy leads to:

$$Q_{\text{pc}} + n_{13}\bar{h}_{13} = n_{10}\bar{h}_{10} + n_{11}\bar{h}_{11} + n_{12}\bar{h}_{12}, \tag{87}$$

where Q_{pc} is the heat released from the post-combustor and used to heat the vaporizer and the pre-heater 1. The exergy balance reads:

$$\begin{aligned} A_{\text{dest,pc}} = &-\left(1 - \frac{T_0}{T_{\text{pc}}}\right) Q_{\text{pc}} + n_{\text{H}_2,10}\bar{a}_{\text{H}_2,10} \\ &+ n_{\text{C}_4\text{H}_{10},10}\bar{a}_{\text{C}_4\text{H}_{10},10} + n_{\text{O}_2,10}\bar{a}_{\text{O}_2,10} + n_{\text{N}_2,10}\bar{a}_{\text{N}_2,10} \\ &+ n_{\text{CO}_2,10}\bar{a}_{\text{CO}_2,10} + n_{\text{CO},10}\bar{a}_{\text{CO},10} + n_{\text{H}_2\text{O},10}\bar{a}_{\text{H}_2\text{O},10} \\ &+ n_{\text{O}_2,11}\bar{a}_{\text{O}_2,11} + n_{\text{N}_2,11}\bar{a}_{\text{N}_2,11} + n_{\text{O}_2,12}\bar{a}_{\text{O}_2,12} \\ &+ n_{\text{N}_2,12}\bar{a}_{\text{N}_2,12} - n_{\text{O}_2,13}\bar{a}_{\text{O}_2,13} - n_{\text{N}_2,13}\bar{a}_{\text{N}_2,13} \\ &- n_{\text{CO}_2,13}\bar{a}_{\text{CO}_2,13} - n_{\text{H}_2\text{O},13}\bar{a}_{\text{H}_2\text{O},13}. \end{aligned} \tag{88}$$

3. Numerical solution

3.1. Fuel cell

The fuel cell model is solved numerically by first choosing the cell voltage E as an iteration parameter. The cell voltage must be between 0 V and the ideal Nernst potential E^0. Since the resulting total overpotential η_{tot} within every discrete element of the

fuel cell depends on the local current density i and the temperature in the air channel, the fuel channel, and the MEA, the entire system of equations needs to be solved iteratively using a Newton algorithm. The integration along the flow direction is accomplished using a fourth-order Runge-Kutta method. For the calculations presented in this study, the results converge fast. For a discretization with 10 spatial steps, the relative error of the resulting exergetic efficiency is 3.5%. For 50, 100, and 200 steps, the relative errors are 0.6, 0.3, and 0.1%. There is no distinguishable deviation for discretizations with more than 500 steps.

3.2. Micro SOFC system

In order to solve for the entire micro SOFC system, the following parameters are prescribed and assumed to be constant: the molar flow rate of butane $n_{C_4H_{10},1}$, the ambient temperature T_0, the temperatures of air and butane before and after pre-heating, the cell voltage E of the SOFC, the cell length L and width b, the extension of reforming ε, and the oxygen/fuel ratios λ_{pox} and λ_{sofc}. With the entire list of parameters given in Table 1, the generated electric power P, all rejected heat Q, and the profiles of temperature, molar concentration, and current density in the SOFC are numerically calculated. The thermodynamic conditions at all states are derived.

4. Results and discussion

In this study, the performance of an SOFC micropowerplant is calculated using operational parameters based on experimental results of several recent studies, as shown in Table 1. It is beyond the purpose of this study to achieve new experimental results for an entire micro SOFC system.

The parameters of the MEA are based on the parameters used in [8,9,14,15], as seen in Table 1. For the anode and the cathode, nickel-doped lanthanum strontium ferrite (LSNF) is used as material for intermediate temperatures. The preparation and the characterization of LSNF are investigated in [14]. The electrolyte consists of a composite of sodium-doped ceria and silica. The electrolyte material for intermediate temperatures and its preparation are characterized in [15]. The parameters needed for matching the experimental data of existing SOFCs [16] are given in Table 1. These studies have shown that satisfactory performance can be achieved for intermediate temperatures between 600 and 1000 K using innovative materials.

The pressure is assumed to be constant at atmospheric conditions and the pressure drop in the channels is neglected. Numerical calculations for the entire micro SOFC system for which a schematic is shown in Fig. 3 are performed. Liquid butane at a molar flow rate $n_{C_4H_{10},1} = 10^{-5}\,\mathrm{mol\,s^{-1}}$, ambient temperature $T_1 = 298\,\mathrm{K}$, and pressure $p_1 = p^{sat}_{C_4H_{10}}(T_1 = 298\,\mathrm{K}) = 2.43\,\mathrm{bar}$ is vaporized isothermally in the vaporizer. Gaseous butane and air are heated in the pre-heater 1 to the temperature of the POX reformer T_{pox}. The POX reformer is assumed to perform isothermally at T_{pox} with an extension of reforming $\varepsilon = 0.9$, a molar ratio between carbon monoxide and carbon dioxide $\varphi_{CO} = 9.0$, and a selectivity for hydrogen $\varphi_{H_2} = 0.9$ [17]. The SOFC is fed by the products of the reforming process and air, where the molar ratio of hydrogen in the fuel gas mixture and oxygen in the air is defined by the air/fuel factor λ_{sofc}. The air is pre-heated in the pre-heater 2, which also changes the temperature of the reformed gas to assure that the fuel inlet temperature T_8 and the air inlet temperature T_9 of the SOFC are the same. The heat-transfer coefficients between the environment and the cathode channel α^c_h and the anode channel α^a_h are assumed to be $1\,\mathrm{W\,m^{-2}\,K^{-1}}$. Modern materials and techniques like vacuum insulation can achieve small heat-transfer coefficients for high temperatures around 1000 K. However, high-temperature insulation presents a major challenge for the development of SOFC micropowerplants. The exhaust of the SOFC is burnt in a post-combustor. It is assumed that heat released from the POX reformer and the post-combustor can be used in the pre-heaters and the vaporizer.

Table 1
Parameters of the standard case

Parameter	Value	Reference
Fuel		
Molar flow rate of butane $n_{C_4H_{10},1}$ (μmol s^{-1})	10	–
Molar enthalpy liquid butane $\bar{h}_{C_4H_{10},1}$ (kJ mol^{-1})	−117.9	[13]
Molar entropy liquid butane $\bar{s}_{C_4H_{10},1}$ (J mol^{-1} K^{-1})	227.8	[13]
Molar availability liquid butane $\bar{a}_{C_4H_{10},1}$ (kJ mol^{-1})	2805.8	[11]
Pre-heaters 1 and 2		
Outer surface area S_{pre} (cm^2)	10.0	–
Heat-transfer coefficient α_{pre} (W m^{-2} K^{-1})	1.0	–
Partial oxidation reformer		
Air/fuel ratio λ_{pox}	2.22	[17]
Extension of reforming ε	0.9	[17]
Carbon monoxide/carbon dioxide ratio φ_{CO}	9.0	[17]
Selectivity of hydrogen φ_{H_2}	0.9	[17]
Solid oxide fuel cell		
Cell length L (m)	0.05	–
Cell width b (m)	0.05	–
Air/fuel ratio λ_{sofc}	1.0	–
Cell voltage E (V)	0.7	–
Heat-transfer coefficient cathode α^c_h (W m^{-2} K^{-1})	1.0	–
Heat-transfer coefficient anode α^a_h (W m^{-2} K^{-1})	1.0	–
Membrane electrolyte assembly		
Average pore radius r (μm)	0.5	[9]
Porosity γ	0.3	[9]
Tortuosity ξ	6	[9]
Anode thickness l_a (μm)	50	[9]
Cathode thickness l_c (μm)	50	[8]
Electrolyte thickness l_{el} (μm)	20	[8]
Activation energy of anode E_a (kJ mol^{-1})	77.2	[14]
Pre-factor of anode $i^0_{0,a}$ (10^{10} A K m^{-2})	15.85	[14]
Activation energy of cathode E_c (kJ mol^{-1})	77.2	[14]
Pre-factor of cathode $i^0_{0,c}$ (10^{10} A K m^{-2})	15.85	[14]
Activation energy E_{el} (kJ mol^{-1})	72.89	[15]
Pre-factor σ_0 (kS m^{-1})	641.5	[15]
All components		
Pressure liquid storage tank p_1 (MPa)	0.243	–
Total pressure p (MPa)	0.1	–
Temperature of environment T_0 (K)	298	–
Temperatures T_1, T_2, T_4, T_7, and T_{12} (K)	298	–
Temperatures T_3, T_5, and T_6 (K)	1000	–
Temperatures T_8 and T_9 (K)	900	–
Temperature T_{10} and T_{11} (K)	633	–
Temperature T_{13} (K)	800	–

Table 2
Energetic results of the standard case

Heat transfer to vaporizer Q_{vap}	0.214 W
Heat transfer to pre-heater 1, Q_{pre1}	4.58 W
Heat transfer to pre-heater 2, Q_{pre2}	1.73 W
Heat transfer from POX reformer Q_{pox}	5.31 W
Heat transfer from post-combustor Q_{pc}	9.24 W
Heat released from SOFC Q_{sofc}	6.80 W
Unused heat from post-combustor Q_{rel1}	4.44 W
Unused heat from POX reformer Q_{rel2}	3.58 W
Heat released from pre-heaters Q_{rel3}	0.885 W
Total heat released to environment Q_{rel}	15.7 W
Temperature of vaporizer T_{vap}	298 K
Temperature of pre-heater 1, T_{pre1}	649 K
Temperature of pre-heater 2, T_{pre2}	833 K
Temperature of POX reformer T_{pox}	1000 K
Temperature of post-combustor T_{pc}	669 K
Temperature of SOFC T_{sofc}	756 K

Table 1 defines all relevant operational and geometric parameters of the entire micro SOFC system. All results are based on these parameters that represent the standard case. Every parameter different from the standard case is mentioned in the text.

Tables 2 and 3 present energetic and exergetic results of the standard case. In Table 2, the heat-transfer rates within the system are quantified. The vaporizer and the pre-heater 1 consume significantly less heat than the post-combustor releases, and the mean temperature of the post-combustor T_{pc} is higher than the temperatures T_{vap} and T_{pre1}. The required heat exchange between these components is therefore possible. The POX reformer rejects more heat than the pre-heater 2 actually needs, and a sufficient temperature difference exists. The assumption that the pre-heaters and the vaporizer can be heated by the heat released from the POX reformer and the post-combustor is therefore feasible. Table 3 presents an exergy analysis of the system. The total exergy destruction by irreversibilities in the system $A_{dest,irr}$ [see Eq. (41)] is caused mainly by the POX reformer, the SOFC, and the post-combustor. The exergy destruction by heat losses $A_{dest,heat}$ is significant. An exergetic efficiency of the entire fuel cell system of 19.4% results.

Table 3
Exergetic results of the standard case

Inlet flow availability	28.1 W
Exergy destruction by vaporizer $A_{dest,vap}$	0.245 W
Exergy destruction by pre-heater 1, $A_{dest,pre1}$	0.00518 W
Exergy destruction by pre-heater 2, $A_{dest,pre2}$	0.528 W
Exergy destruction by POX reformer $A_{dest,pox}$	3.29 W
Exergy destruction by SOFC $A_{dest,sofc}$	3.75 W
Exergy destruction by post-combustor $A_{dest,pc}$	4.51 W
Exergy destruction by irreversibility $A_{dest,irr}$	12.3 W
Exergy destruction by heat transfer $A_{dest,heat}$	7.24 W
Outlet flow availability a_{13}	3.11 W
Useful electric power P	5.45 W
Exergetic efficiency of the entire system μ	19.4%
Hydrogen utilization factor U_{H_2}	100.0%

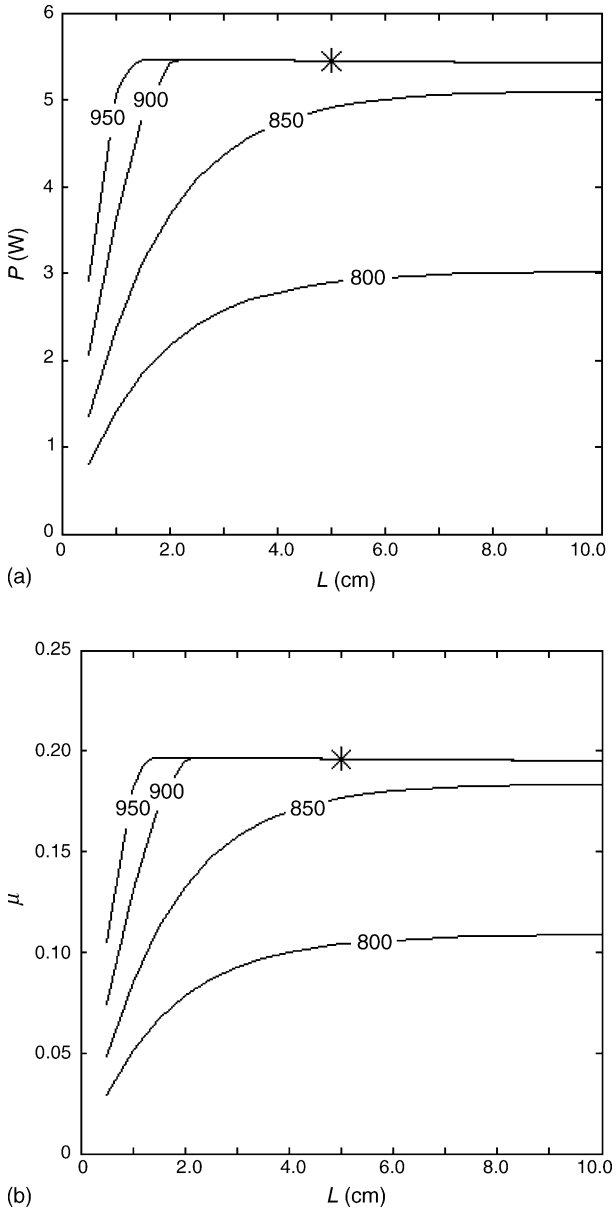

Fig. 4. (a) Electric power P as a function of cell length L for different SOFC inlet temperatures T_8. Labels indicate T_8 in K. All other operational parameters are taken from the standard case. (b) Exergetic efficiency μ as a function of cell length L for different SOFC inlet temperatures T_8.

In the standard case, a cell length $L = 5$ cm is chosen. In order to investigate the dependence of the power P on the cell length L, the performance of the fuel cell system is calculated for different cell lengths L and various fuel and air inlet temperatures T_8. In Fig. 4(a), the electric power P is plotted as a function of the cell length L for different inlet temperatures T_8. The star marks the result of the standard case. The longer the fuel cell, the higher the electric power P is. However, the performance increase strongly depends on the fuel cell inlet temperature. For high T_8, a maximum power of about 5.45 W is reached for quite small cell lengths. A fuel cell with operational parameters of the standard case could have a length of 2 cm instead of 5 cm without any power loss for high inlet temperatures. For lower temperatures T_8, the maximum power of 5.1 W for $T_8 = 850$ K and 3.0 W

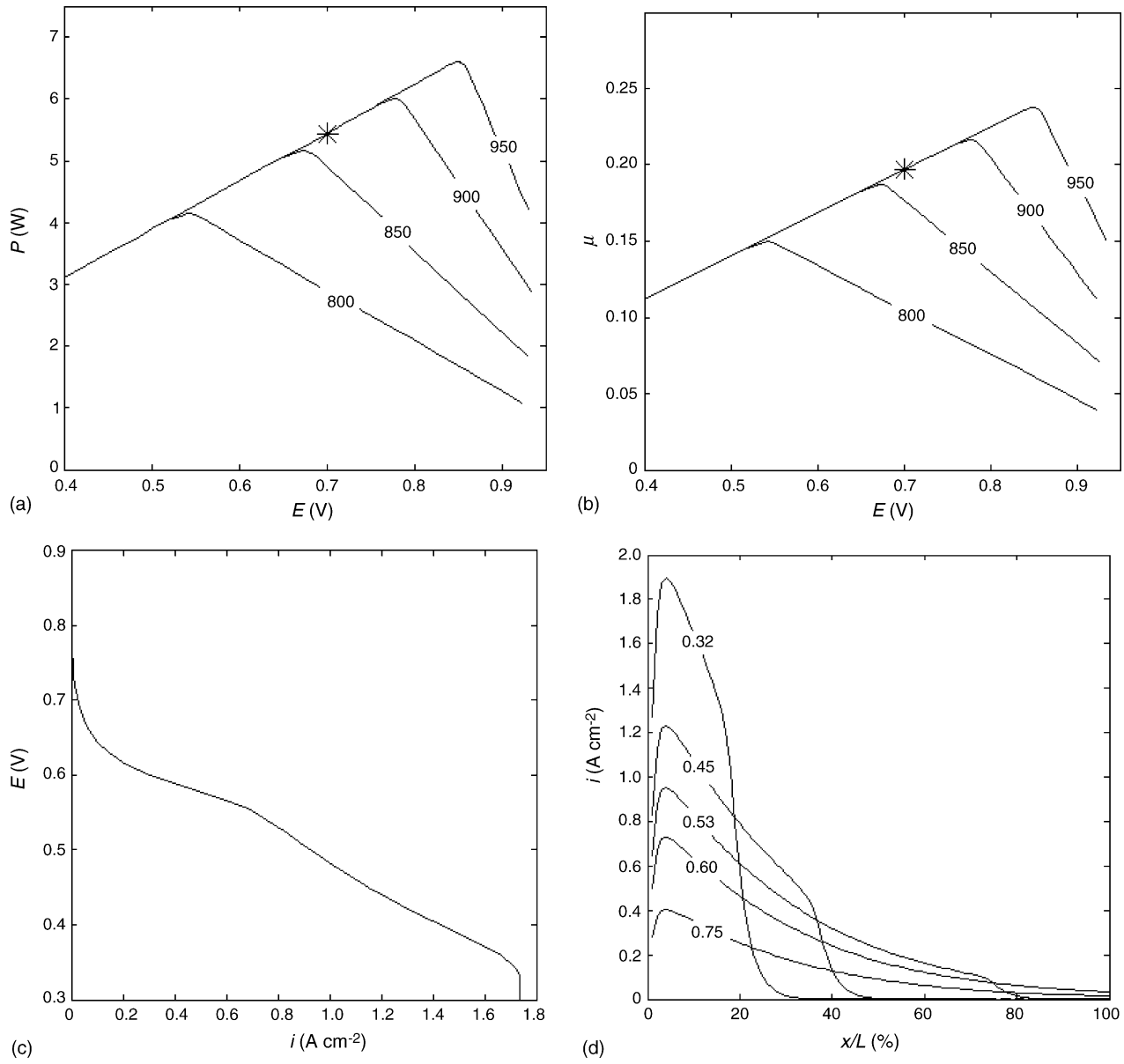

Fig. 5. (a) Electric power P as a function of cell voltage E for different SOFC inlet temperatures T_8. Labels indicate T_8 in K. (b) Exergetic efficiency μ as a function of cell voltage E for different SOFC inlet temperatures T_8. (c) Cell voltage E as a function of the current density i for $T_8 = 800$ K. (d) Current density profiles i along the fuel cell for $T_8 = 800$ K and different cell voltages E.

for $T_8 = 800$ K is reached for cell lengths above 7 cm. Fig. 4(b) shows the corresponding exergetic efficiency μ. The maximum efficiency amounts to 19.4%. Even if $T_8 = 850$ K, an exergetic efficiency of 18% is possible for longer cells. If $T_8 = 800$ K, a maximum efficiency of about 11% results.

Fig. 5 shows the effect of the cell voltage E on the performance of the fuel cell system. In the standard case, $E = 0.7$ V applies. The electric power P changes as a function of the cell voltage E, according to Fig. 5(a). The labels indicate the SOFC inlet temperature T_8. The star marks the result of the standard case. The power P increases linearly with the cell voltage, independent on the inlet temperature T_8, until a maximum value is reached. The lower T_8, the lower is this maximum and the lower is the cell voltage E where the maximum is obtained. For cell voltages higher than the maximum value, the power drops rapidly. This drop is again almost linear, with different slopes for different temperatures. This result supports a careful choice of the operating cell voltage, because the power might drop by more than 1 W for a change of cell voltage of only 0.1 V, especially for higher temperatures T_8. In Fig. 5(b), the exergetic efficiency μ is given as a function of the cell voltage E for different SOFC inlet temperatures T_8.

An interesting aspect of Fig. 5(a) and (b) is the abrupt decrease of power after the maximum, giving the graphs an almost triangular shape. Fig. 5(c) describes one reason for this phenomenon. The typical voltage–current curve is shown for $T_8 = 800$ K. At a cell voltage E of about 0.55 V, the slope of the voltage–current curve changes. This happens near the voltage where the maximum power P is achieved. For higher voltages than 0.55 V, the curve is dominated by activation overpotentials,

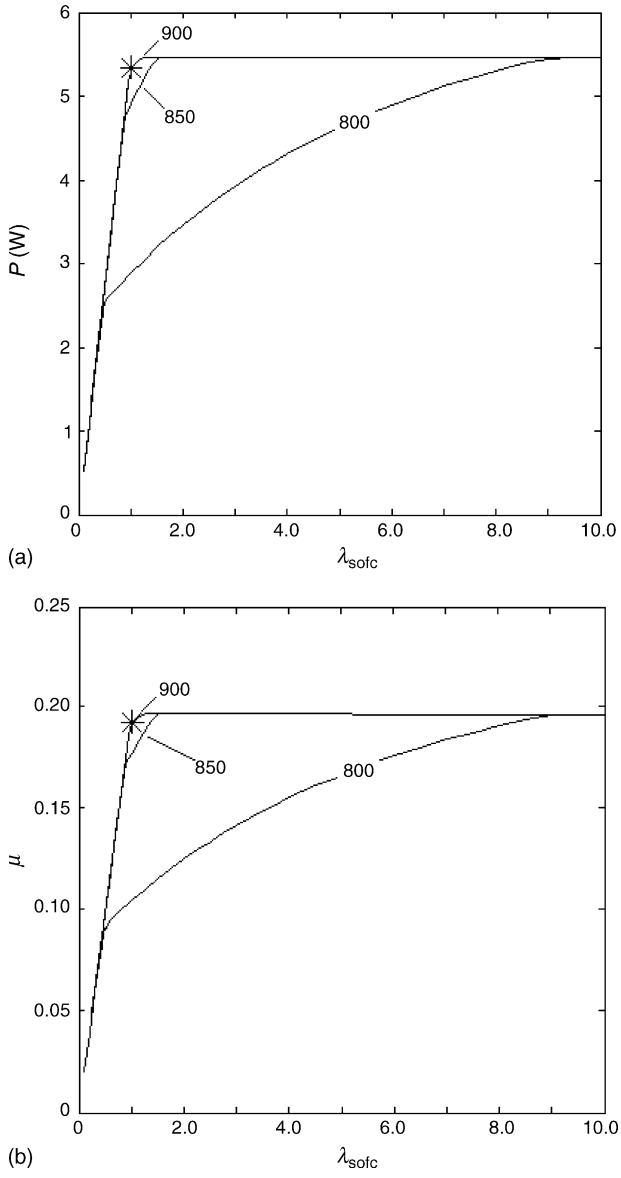

Fig. 6. (a) Electric power P as a function of the air/fuel ratio λ_{sofc} for different SOFC inlet temperatures T_8. Labels indicate T_8 in K. All other operational parameters are taken from the standard case. (b) Exergetic efficiency μ as a function of the air/fuel ratio λ_{sofc} for different SOFC inlet temperatures T_8.

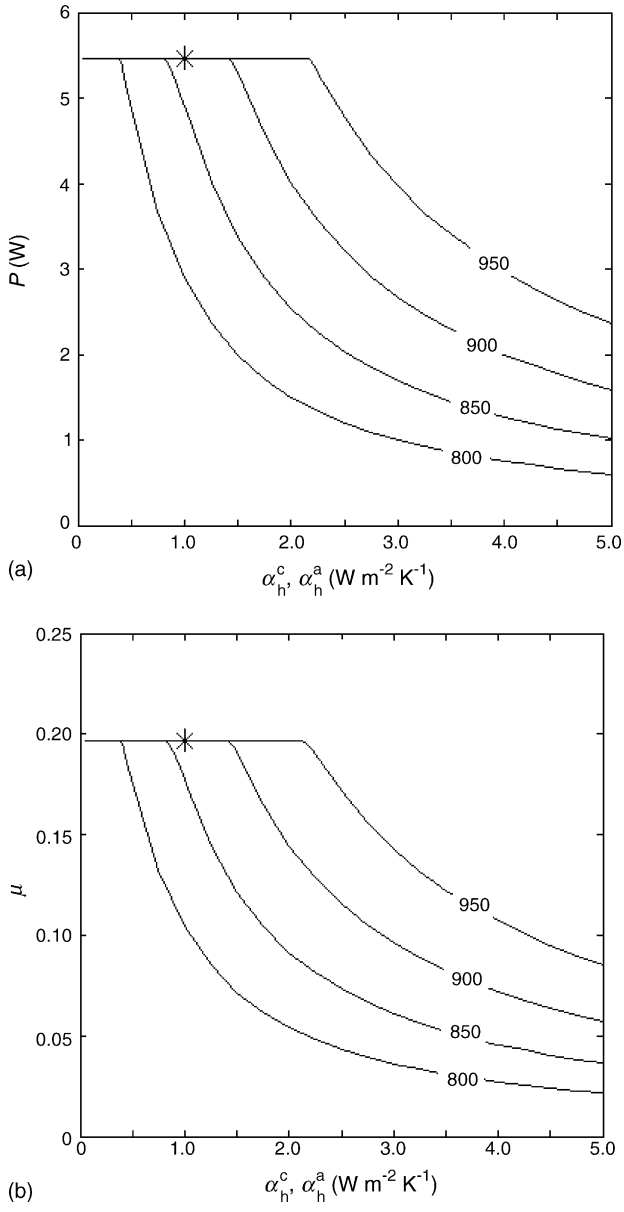

Fig. 7. (a) Electric power P as a function of the heat-transfer coefficients α_h^c and α_h^a for different SOFC inlet temperatures T_8. Labels indicate T_8 in K. All other operational parameters are taken from the standard case. (b) Exergetic efficiency μ as a function of the heat-transfer coefficients α_h^c and α_h^a for different SOFC inlet temperatures T_8.

whereas for smaller cell voltages, the curve is mainly defined by ohmic losses. This effect is intensified by another phenomenon, shown in Fig. 5(d). This plot presents the current density profiles i along the fuel cell for $T_8 = 800$ K and different cell voltages E. For all cell voltages, the maximum current density is achieved close to the beginning of the fuel cell. For smaller voltages, the current density drops dramatically to zero at a certain point, because all hydrogen is consumed. The higher the cell voltage, the more the point with $i \approx 0$ moves towards the end of the fuel cell. For cell voltages $E > 0.55$ V, the fuel cell is too short to convert all hydrogen.

Another important operating parameter is the air/fuel ratio λ_{sofc}. In Fig. 6(a), the electric power P is plotted as a function of the air/fuel ratio λ_{sofc} for different SOFC inlet temperatures T_8. The labels indicate the temperature T_8. The electric power increases linearly if $\lambda_{sofc} < 0.5$, independent on temperature. In this region, the air supply determines the achievable power. If $T_8 \geq 900$ K, a maximum power of about 5.5 W is reached for air/fuel ratios slightly higher than 1.0. Further increase of the air inlet flow rate leads to no further increase in power, since the performance is limited by the hydrogen supply in this operating region. For lower temperatures T_8, the air/fuel ratio affects the performance more severely. If $T_8 = 800$ K, a maximum power of 5.5 W can be reached, if λ_{sofc} is increased to a value of 9.0. A high air inlet flow rate can therefore decrease the necessary SOFC inlet temperature T_8 significantly. Fig. 6(b) shows the exergetic efficiency μ as a function of the air/fuel ratio λ_{sofc} for different SOFC inlet temperatures T_8.

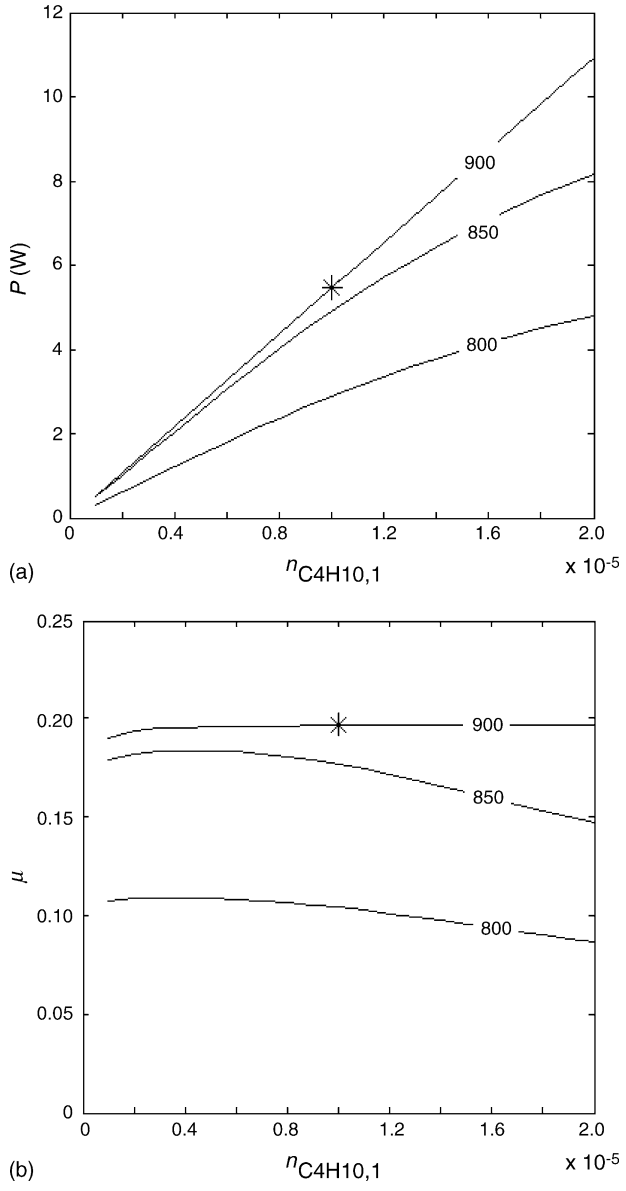

Fig. 8. (a) Electric power P as a function of the inlet molar flow rate of butane $n_{C_4H_{10},1}$ for different SOFC inlet temperatures T_8. Labels indicate T_8 in K. All other operational parameters are taken from the standard case. (b) Exergetic efficiency μ as a function of the inlet molar flow rate of butane $n_{C_4H_{10},1}$ for different SOFC inlet temperatures T_8.

For the standard case, the heat-transfer coefficients between environment and cathode channel α_h^c and anode channel α_h^a are both set to 1 W m^{-2} K^{-1}. These parameters have a strong influence on the electric power and the efficiency of the fuel cell system. In Fig. 7(a), the electric power P is plotted as a function of the heat-transfer coefficients α_h^c and α_h^a for different SOFC inlet temperatures T_8. The labels indicate the temperature T_8. All other operational parameters are taken from the standard case presented in Table 1. The star marks the result of the standard case. For small heat-transfer coefficients, indicating a good insulation of the fuel cell, a maximum power of about 5.45 W is reached for all temperatures. For a low SOFC inlet temperature of 800 K, the power P starts to drop for heat-transfer coefficients below 0.5 W m^{-2} K^{-1}. If $T_8 > 900$ K, the drop starts above 2.0 W m^{-2} K^{-1}. The performance loss is remarkable. The achievable power P can almost be doubled for $T_8 = 800$ K by improving the insulation from 1.0 to 0.5 W m^{-2} K^{-1}. This may offer another possibility to decrease the operating temperature of the SOFC without losing electric power. In Fig. 7(b), the exergetic efficiency μ is presented as a function of the heat-transfer coefficients α_h^c and α_h^a for different SOFC inlet temperatures T_8.

A final analysis shows the dependence of the performance of the entire fuel cell system on the molar flow rate of liquid butane $n_{C_4H_{10},1}$. In Fig. 8(a), the electric power P is plotted as a function of the inlet molar flow rate of liquid butane $n_{C_4H_{10},1}$ for different SOFC inlet temperatures T_8. The labels indicate the temperature T_8. All other operational parameters are taken from the standard case presented in Table 1. The star marks the result of the standard case. For SOFC inlet temperatures $T_8 \geq 900$ K, the power increases almost linearly with the molar flow rate of butane, since all hydrogen is converted in the fuel cell. For lower temperatures, the performance of the fuel cell is too low to use all available hydrogen. In Fig. 8(b), the exergetic efficiency μ is shown as a function of the inlet molar flow rate of butane $n_{C_4H_{10},1}$ for different SOFC inlet temperatures T_8. For $T_8 = 900$ K, the exergetic efficiency μ is almost constant within the plotted range.

The results of this study show that the fuel cell performance can be easily increased by adjusting the operating parameters. For the standard case with a SOFC inlet temperature $T_8 = 900$ K, the power P can be enhanced by slightly changing the cell voltage E to 0.78 V and the air/fuel ratio λ_{sofc} to 1.2. These small adjustments lead to an optimum electric power of 6.1 W, compared to 5.45 W in the standard case. The exergetic efficiency μ rises to 21.9%. The results demonstrate possibilities to achieve satisfactory power for SOFC inlet temperatures $T_8 < 900$ K. By using the parameters of the standard case and only changing the SOFC inlet temperature T_8 to 800 K, the power drops to 2.9 W. However, by changing the cell voltage to 0.55 V, increasing the air/fuel ratio λ_{sofc} to 2.0, and improving the heat-transfer coefficients α_h^c and α_h^a to 0.5 W m^{-2} K^{-1}, the power P reaches 4.3 W. The exergetic efficiency amounts to 15.4% in this case.

5. Conclusions

The fuel cell micropowerplant model developed in this study replicates the characteristic behavior of a SOFC system under a host of operating conditions. The influence of operational and geometric parameters on the efficiency of a micro SOFC system is investigated according to the first and the second law of thermodynamics. It is shown that the exergetic efficiency of the system can be increased significantly by proper choice of operating conditions. Useful information about such optimal conditions can be deduced from the model presented in this study. The developed fuel cell model can be modified and extended to consider different types of fuels or different system configurations. Further improvement could be achieved by extending the simplified flow model in the fuel cell channels and by using a more complex heat-transfer model. Nevertheless all relevant physics is covered by the present model. An

interesting approach might be the simultaneous conversion of different species in the fuel cell instead of single usage of hydrogen.

Appendix A

The activation polarizations $\eta_{act,a}$ and $\eta_{act,c}$ are expressed by Butler–Volmer equations [7,9,18]. The activation polarization of the anode and cathode is given as [9]:

$$\eta_{act,a} = \frac{2RT}{n_e F} \operatorname{ar\,sinh}\left(\frac{i}{2i_{0,a}}\right) \tag{A.1}$$

and

$$\eta_{act,c} = \frac{2RT}{n_e F} \operatorname{ar\,sinh}\left(\frac{i}{2i_{0,c}}\right), \tag{A.2}$$

respectively, where n_e indicates the number of electrons transferred in a single elementary rate-limiting step and a common assumption is $n_e = 1$ [8]. The current density is represented by i and the exchange current densities $i_{0,a}$ and $i_{0,c}$ are the electrode reaction rates at the equilibrium potential. In order to account for the temperature dependence of the exchange current densities, the exchange current densities are modeled as [14]:

$$i_{0,a} = \frac{i^0_{0,a}}{T} \exp\left(-\frac{E_a}{RT}\right) \tag{A.3}$$

for the anode, and

$$i_{0,c} = \frac{i^0_{0,c}}{T} \exp\left(-\frac{E_c}{RT}\right) \tag{A.4}$$

for the cathode, using Arrhenius type coefficients $i^0_{0,a}$, $i^0_{0,c}$, E_a, and E_c extracted from Table 1 of Ref. [14].

The concentration polarizations $\eta_{conc,a}$ and $\eta_{conc,c}$ describe the resistances for mass diffusion through the porous electrodes. In the anode, 1D equimolar diffusion of hydrogen and water takes place at steady state, where the molar fluxes are functions of molar concentration gradients and the effective binary diffusion coefficient $D_{eff,a}$. By combining the definitions of molar fluxes of hydrogen and water, the concentration polarization for the anode is [9]:

$$\eta_{conc,a} = -\frac{RT}{2F} \ln\left(\frac{1 - (l_a/2FD_{eff,a}c^a_{H_2,h})i}{1 + (l_a/2FD_{eff,a}c^a_{H_2O,h})i}\right), \tag{A.5}$$

where l_a is the anode thickness. The concentration polarization of the cathode reads [9]:

$$\eta_{conc,c} = -\frac{RT}{4F} \ln\left[\frac{(p/\delta_{O_2}) - ((p/\delta_{O_2}) - RTc^c_{O_2,h})\exp(RT\delta_{O_2}l_c i/4FD_{eff,c}p)}{RTc^c_{O_2,h}}\right], \tag{A.6}$$

where l_c is the cathode thickness and $c^c_{O_2,h}$ the molar concentration of oxygen in the cathode channel. The factor δ_{O_2} is the ratio of Knudsen diffusion and the sum of binary ordinary diffusion and Knudsen diffusion. The effective diffusion coefficient of the anode $D_{eff,a}$ is calculated by using the diffusion coefficients of hydrogen and water, given as [9]:

$$D_{eff,a} = \frac{c^a_{H_2O,h}D_{eff,H_2} + c^a_{H_2,h}D_{eff,H_2O}}{c^a_{H_2O,h} + c^a_{H_2,h}}. \tag{A.7}$$

The diffusion coefficient of hydrogen [9],

$$D_{eff,H_2} = (D^{-1}_{eff,H_2,K} + D^{-1}_{eff,H_2-H_2O})^{-1} \tag{A.8}$$

and the diffusion coefficient of water [9]

$$D_{eff,H_2O} = (D^{-1}_{eff,H_2O,K} + D^{-1}_{eff,H_2-H_2O})^{-1} \tag{A.9}$$

represent a combination of Knudsen diffusion and binary ordinary diffusion. The Knudsen diffusion coefficients [19],

$$D_{eff,H_2,K} = \frac{2}{3} \times 10^{1.5} r \frac{\gamma}{\xi}\sqrt{\frac{8RT}{\pi M_{H_2}}} \tag{A.10}$$

and

$$D_{eff,H_2O,K} = \frac{2}{3} \times 10^{1.5} r \frac{\gamma}{\xi}\sqrt{\frac{8RT}{\pi M_{H_2O}}} \tag{A.11}$$

of hydrogen and water, respectively, are functions of the temperature T, the molar mass of the gas M, and the average pore radius r of the anode. In order to take into account the tortuous path of the diffusing gases and the porosity of the electrodes, the effective diffusion coefficients are multiplied with the ratio of the porosity γ and the tortuosity ξ. The binary ordinary diffusion coefficient in $m^2\,s^{-1}$ is calculated according to the Chapman-Enskog equation, given as [20]:

$$D_{eff,H_2-H_2O} = 1.8583 \times 10^{-7}\, T^{1.5} \frac{([1/M_{H_2}] + [1/M_{H_2O}])^{1/2}}{p\sigma^2_{H_2-H_2O}\Omega_{H_2-H_2O}} \times \frac{\gamma}{\xi}. \tag{A.12}$$

Herein, p is the pressure in atmospheres. The collision diameter $\sigma_{H_2-H_2O}$ with units in angstrom and the collision integral $\Omega_{H_2-H_2O}$ are based on the Lennard-Jones potential [21]. Similarly, the effective diffusion coefficient of the cathode $D_{eff,c}$ is a combination of Knudsen diffusion and binary ordinary diffusion [9]

$$D_{eff,c} = D_{eff,O_2} = (D^{-1}_{eff,O_2,K} + D^{-1}_{eff,O_2-N_2})^{-1} \tag{A.13}$$

and δ_{O_2} is the ratio of these two diffusion parts [9]:

$$\delta_{O_2} = \frac{D_{eff,O_2,K}}{D_{eff,O_2,K} + D_{eff,O_2-N_2}}. \tag{A.14}$$

The Knudsen diffusion coefficient of oxygen is given as [19]:

$$D_{\mathrm{eff,O_2,K}} = \frac{2}{3} \times 10^{1.5}\, r \frac{\gamma}{\xi} \sqrt{\frac{8RT}{\pi M_{\mathrm{O_2}}}} \tag{A.15}$$

and the binary ordinary diffusion coefficient in $\mathrm{m^2\,s^{-1}}$ reads [20]:

$$D_{\mathrm{eff,O_2-N_2}} = 1.8583 \times 10^{-7}\, T^{1.5} \frac{([1/M_{\mathrm{O_2}}] + [1/M_{\mathrm{N_2}}])^{1/2}}{p\sigma^2_{\mathrm{O_2-N_2}} \Omega_{\mathrm{O_2-N_2}}} \times \frac{\gamma}{\xi}. \tag{A.16}$$

The last polarization considers ohmic losses due to transport of ions in the electrolyte. Ohmic losses in the electrodes are much smaller, and are therefore neglected. The electric current in the electrolyte obeys Ohm's law,

$$\eta_{\mathrm{ohm}} = R_{\mathrm{el}} i. \tag{A.17}$$

Taking into account the dependence on temperature, the specific ohmic resistance of the electrolyte R_{el} can be expressed as [7]:

$$R_{\mathrm{el}} = \frac{l_{\mathrm{el}}}{\sigma_{\mathrm{el}}} = \frac{l_{\mathrm{el}}}{\sigma_0} \exp\left(\frac{E_{\mathrm{el}}}{RT}\right), \tag{A.18}$$

where l_{el} refers to the thickness of the electrolyte, E_{el} the activation energy of the ionic transport, and σ_0 a reference ionic conductivity. The coefficients σ_0 and E_{el} are extracted from Fig. 8 of Ref. [15].

References

[1] M.A. Rosen, Comparison based on energy and exergy analyses of the potential cogeneration efficiencies for fuel cells and other electricity generation devices, Int. J. Hydrogen Energy 15 (1990) 267–274.

[2] S.L. Douvartzides, F.A. Coutelieris, P.E. Tsiakaras, On the optimization of ethanol fed SOFC-based electricity generating systems in terms of energy and exergy, J. Power Sources 114 (2003) 203–212.

[3] P.E. Tsiakaras, A. Demin, Thermodynamic analysis of a solid oxide fuel cell system fuelled by ethanol, J. Power Sources 102 (2001) 210–217.

[4] S.L. Douvartzides, F.A. Coutelieris, P.E. Tsiakaras, Exergy analysis of a solid oxide fuel cell power plant fed by either ethanol or methane, J. Power Sources 131 (2004) 224–230.

[5] S.L. Douvartzides, P.E. Tsiakaras, Thermodynamic and economic analysis of a steam reformer-solid oxide fuel cell system fed by natural gas and ethanol, Energy Sources 24 (2002) 365–373.

[6] K.W. Bedringås, I.S. Ertesvåg, S. Byggstøyl, B.F. Magnussen, Exergy analysis of solid-oxide fuel-cell (SOFC) systems, Energy 22 (1997) 403–412.

[7] S.H. Chan, C.F. Low, O.L. Ding, Energy and exergy analysis of simple solid-oxide fuel-cell power systems, J. Power Sources 103 (2002) 188–200.

[8] H. Zhu, R.J. Kee, A general mathematical model for analyzing the performance of fuel-cell membrane-electrode assemblies, J. Power Sources 117 (2003) 61–74.

[9] S.H. Chan, K.A. Khor, Z.T. Xia, A complete polarization model of a solid oxide fuel cell and its sensitivity to the change of cell component thickness, J. Power Sources 93 (2001) 130–140.

[10] M.J. Moran, H.N. Shapiro, Fundamentals of Engineering Thermodynamics, fourth ed., Wiley, 1999.

[11] D.R. Morris, J. Szargut, Standard chemical exergy of some elements and compounds on the planet earth, Int. J. Energy 11 (1986) 733–755.

[12] M.W. Chase, NIST-JANAF thermochemical tables, fourth edition, J. Phys. Chem. Ref. Data, Monograph 9 (1998) 1–1951.

[13] J.G. Aston, G.H. Messerly, The heat capacity and entropy, heats of fusion and vaporization and the vapor pressure of *n*-butane, J. Am. Chem. Soc. 62 (1940) 1917–1923.

[14] G.W. Coffey, J.S. Hardy, L.R. Pederson, P.C. Rieke, E.C. Thomsen, Oxygen reduction activity of lanthanum strontium nickel ferrite, Electrochem. Solid-State Lett. 6 (2003) A121–A124.

[15] B. Zhu, Functional ceria–salt-composite materials for advanced ITSOFC applications, J. Power Sources 114 (2003) 1–9.

[16] B. Zhu, X.T. Yang, J. Xu, Z.G. Zhu, S.J. Ji, M.T. Sun, J.C. Sun, Innovative low temperature SOFCs and advanced materials, J. Power Sources 118 (2003) 47–53.

[17] A.S. Bodke, S.S. Bharadwaj, L.D. Schmidt, The effect of ceramic supports on partial oxidation of hydrocarbons over noble metal coated monoliths, J. Catalysis 179 (1998) 138–149.

[18] C. Berger, Handbook of Fuel Cell Technology, Prentice-Hall, Englewood Cliffs, NJ, 1968.

[19] C.V. Heer, Statistical Mechanics, Kinetic Theory, and Stochastic Processes, Academic Press (1972).

[20] R.B. Bird, W.E. Stewart, E.N. Lightfoot, Transport Phenomena, Wiley, 1960, p. 511.

[21] E.L. Cussler, Diffusion Mass Transfer in Fluid Systems, second ed., Cambridge University Press, 1997.